Trackbed settlement and associated ballast degradation due to repeated train moving loads

Citation for published version:
Gu, Q, Zhao, C, Bian, X, Morrissey, JP & Ooi, J 2022, 'Trackbed settlement and associated ballast degradation due to repeated train moving loads', *Soil Dynamics and Earthquake Engineering*, vol. 153, 107109. https://doi.org/10.1016/j.soildyn.2021.107109

Digital Object Identifier (DOI):
10.1016/j.soildyn.2021.107109

Link:
Link to publication record in Edinburgh Research Explorer

Document Version:
Peer reviewed version

Published In:
Soil Dynamics and Earthquake Engineering

Trackbed Settlement and Associated Ballast Degradation Due to Repeated Train Moving Loads

Qiusheng Gu
Doctoral student, Key Laboratory of Soft Soils and Geoenvironmental Engineering, MOE, Department of Civil Engineering, Zhejiang University, Hangzhou 310058, China. Email: qiusheng@zju.edu.cn

Chuang Zhao
Ph.D., Research Associate, Key Laboratory of Soft Soils and Geoenvironmental Engineering, MOE, Department of Civil Engineering, Zhejiang University, 310058, China. Email: zhaochuang@zju.edu.cn

Xuecheng Bian* (Corresponding author)
Ph.D., Professor, Key Laboratory of Soft Soils and Geoenvironmental Engineering, MOE, Department of Civil Engineering, Zhejiang University, Hangzhou 310058, China. Email: bianxc@zju.edu.cn

John Paul Morrissey
Ph.D., Research Associate, Institute for Infrastructure and Environment, School of Engineering, The University of Edinburgh, Scotland, U.K, EH9 3JL. Email:J.Morrissey@ed.ac.uk

Jin Yeam Ooi
Ph.D., Professor, Institute for Infrastructure and Environment, School of Engineering, The University of Edinburgh, Scotland, U.K, EH9 3JL. Email: J.Ooi@ed.ac.uk

Abstract

With increasing train speed and wheel axle load, severe vibrations can occur in a ballasted trackbed, thereby accelerating the degradation of the ballast particles and ultimately causing excessive settlement. To gain insights into the long-term trackbed behavior and the ballast degradation evolution, a full-scale ballasted track experiment with eight sleepers was designed and tested on a validated physical model test platform (ZJU-iHSRT). Sieving analysis together with computer-aided ballast morphology analysis were adopted to quantify the ballast degradation in terms of both the ballast particle size and morphological evolution, after every 100,000 train carriages. Various sensors were installed at key locations in the trackbed to record the dynamic stress responses, vibration velocities and deformations under train moving loads for up to 500,000 train carriages in total. The movements of individual particles inside the ballast layer were also captured using "SmartRock" wireless sensors. The dynamic soil stresses and vibration velocities in the trackbed all peaked at the locations underneath the rail seat and decayed with the distance away from the rail seat. Severe ballast degradation occurred in both particle sizes and morphological properties, with the ballast particles in the middle zone under the sleeper suffering a greater breakage due to the stronger confinement. The long-term train loads densified the ballast layer, both through particle rearrangement and particle breakage filling the voids in the ballast bed, resulting in a reduction in the stresses and vibrations. The amplitudes of the vertical stresses and the vibration velocities in the trackbed around the rail seat were reduced by over 25% and 38% respectively after 500,000 train loading carriages. The ballast particle shape became more compact after the test, with larger diameter and more Platy, Bladed and Elongate shapes found to be the more likely to degrade. Over 50% of the permanent settlement of the ballasted trackbed resulted from the ballast layer deformation, and the increase in the train speed intensified particle movements away from the sleeper in the lateral and longitudinal directions in the ballast layer and accelerated the development of the accumulated settlement, while the increase in the axle load

caused the ballast breakage index (BBI) to rise dramatically by over 50 % and contributed significantly to a greater settlement.

Keywords: Trackbed settlement; Train moving load; Ballast degradation; Full-scale test; High-speed railway.

1. Introduction

Ballasted track is a traditional railway structure that can be divided into the superstructure comprising of the rail, fastener and sleeper, sitting on the trackbed substructure comprising of the ballast layer, subballast layer and subgrade. The trackbed is intended to reduce the effect of the train traffic load transferred from the superstructure whilst minimising the potential damage that could occur for the relatively fragile trackbed. However, the recent increase of train speeds and axle loads has produced significantly higher dynamic responses and vibrations in ballasted track, which could eventually cause excessive cumulative deformation and reduced long-term performance. Therefore, the study of the ballasted track behavior and ballast degradation under the long-term train loads of increased train speed and axle load is of great significance to provide better understanding for preventing track deterioration and improving long-term performance.

The trackbed of ballasted track plays a key role in absorbing the train traffic load and providing lateral restraints to reduce the track deformation, but the increase of train speed and axle load can intensify the dynamic stresses in the subgrade and accelerate the deterioration of the track structure [1]. Some triaxial test results have indicated that an increase of the train speed (loading frequency) would cause plastic collapse and excessive deformation [2-4], while an increase in the axle load would decrease the initial confining pressure in the ballast bed and result in greater vertical and lateral deformations [5]. Ballast specimens in laboratory testing have been reported to exhibit a “liquefaction” phenomenon due to more extensive particle sliding and rolling under the higher vibration loads, which could result in decreasing stability of the specimens [4, 6]. Field test results have shown that the peak vertical and lateral stresses in the ballast bed rise with higher axle loads, and the effect of increased train speed is more pronounced at the sleeper-ballast interface [7]. Nevertheless, previous studies could not reveal the long-term ballasted track behavior for the increased train speed and axle load as the experiments were often conducted with significant limitation of the physical and time scales. A large scale indoor physical model is a good long-term test method that considers the issues of time and cost whilst addressing the low reliability and weather conditions faced by field tests. This paper reports on a new series of experiments using the full-scale physical model test platform (Zhejiang University High-Speed Rail Tester: ZJU-iHSRT) capable of reproducing moving train traffic loads with a maximum axle load of 25 tonnes and a maximum speed of 360 km/h [8, 9] where its reliability has been previously verified by comparison with the actual measurement results [10, 11].

Ballast degradation (ballast breakage and abrasion) induced by train traffic is one of the primary reasons for excessive settlement and reduced track performance [12]. It has been demonstrated that gradation and morphological characteristics have a significant influence on the mechanical properties and deformation of granular materials like ballast [13-15]. Moreover, the reduced internal friction angle arising probably from the decrease in the interlocking effect caused by ballast degradation contribute to the decrease of a track's rigidity, stability and bearing capacity [16, 17]. It has also been shown that the degradation of granular materials depends on the effective lateral restraint stress and the material properties [18-20], and the morphological characteristics have a significant impact on the ballast degradation process [21-25]. Most recent studies are focused on the breakage and abrasion of ballast particles using the Los Angeles abrasion test or ballast triaxial test, which cannot replicate the degradation process of ballast particles under a real train load [26]. Thus, it is necessary to explore trends or mechanisms of ballast degradation from a moving train load. Particle movement also plays an important role in the deformation of a ballast layer, but it is difficult to capture the ballast movement characteristics at a particle scale. An innovative "SmartRock" wireless sensor that uses a built-in three-axis gyroscope, accelerometer, and magnetometer to record particle rotation and translation in real-time is deployed [27, 28]. The reliability of this type of sensor was verified elsewhere both in the triaxial test and in-situ [29, 30].

In this study, a physical full-scale ballasted track was constructed in a laboratory using the Zhejiang University High-Speed Rail Tester (ZJU-iHSRT), and the development of dynamic soil stresses, vibration velocities and deformations, and particle-scale ballast movement characteristics provided by the "SmartRock" sensors are presented and discussed. A sieving analysis together with a computer-aided ballast morphology analysis were performed to study the ballast degradation evolution of both the particle size and shape characteristics over a relatively long duration of cyclic load of up to 500,000 train carriage passages.

2. Full-scale ballasted railway model test

2.1. Test apparatus and ballasted track structure

The full-scale ballasted track in this study was built inside a large rectangular metal box (length 15 m, width 5.5 m) as shown in Fig. 1. A 15 mm-thick smooth latex layer is spread on the inner walls of the metal box to improve the structural damping and minimize the boundary effects. The full-scale ballasted track established in the test comprised eight sleepers (spaced at 63 cm), while a 30 cm-thick ballast layer, 60 cm-thick subballast layer, and a 205 cm-thick clay subgrade were set below. Before the loading phase, the trackbed was compacted with a tamping machine layer by layer to the required stiffness of the Chinese High-speed Railway Design Code (TB 10621-2014), which were constructed in the same manner as in the field. Static plate load tests (K30 tests) using a circular plate with a diameter of 30 cm were carried out to measure the trackbed stiffness after each layer was filled and compacted. In order to achieve the required sleeper support stiffness (120 kN/mm), ballast tamping was also conducted by applying static load and sinusoidal dynamic load to compact the ballast bed under the sleeper during placement. The slopes of the ballast layer and its underlying roadbed were 1:1.75 and 1:1.50, respectively. The particle size distribution (PSD) and the properties of the geomaterials used in the test are shown in Fig. 2 and Table 1.

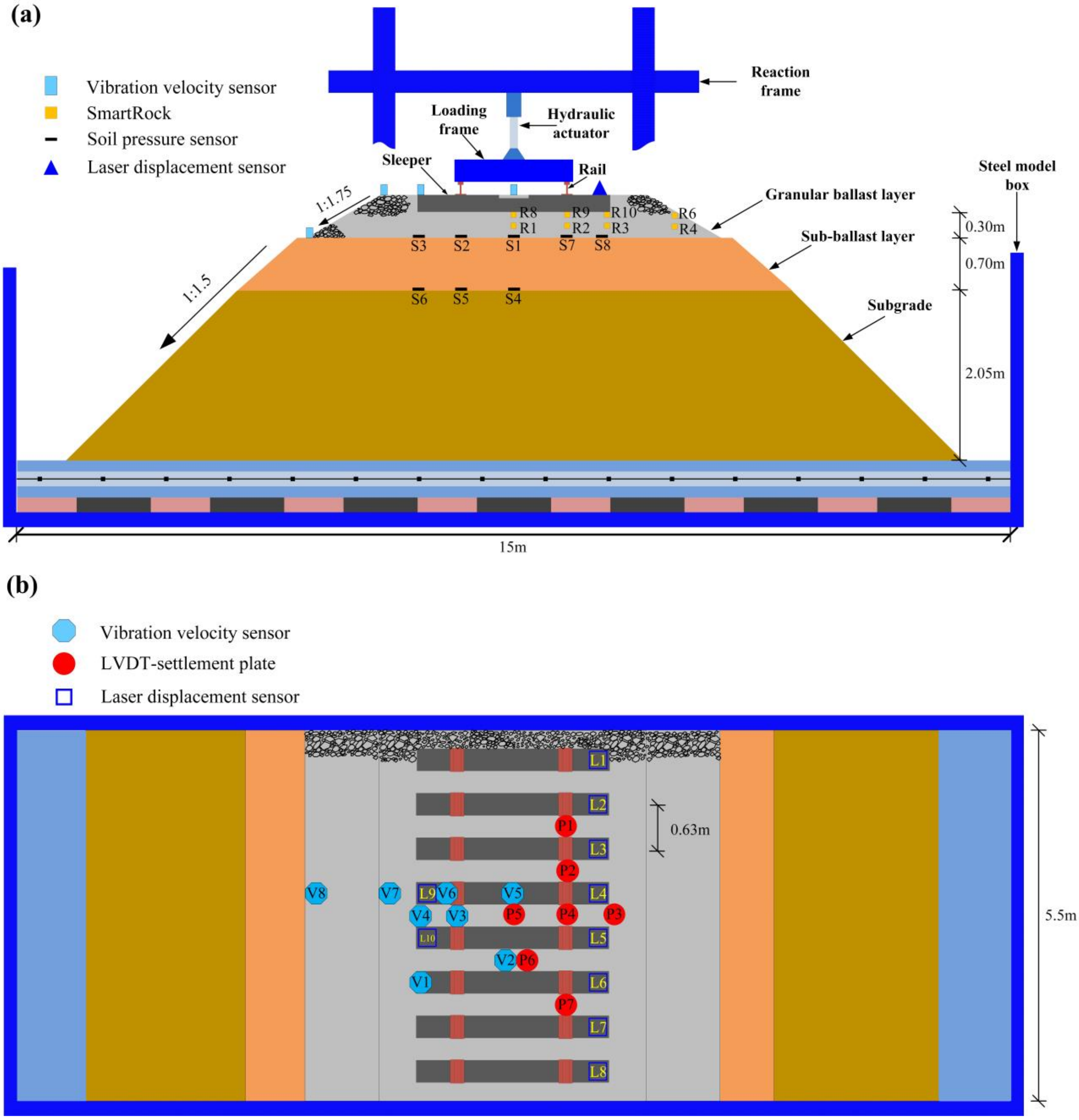

Figure 1. ZJU-iHSRT and ballasted track layout: (a) transverse view; (b) top view.

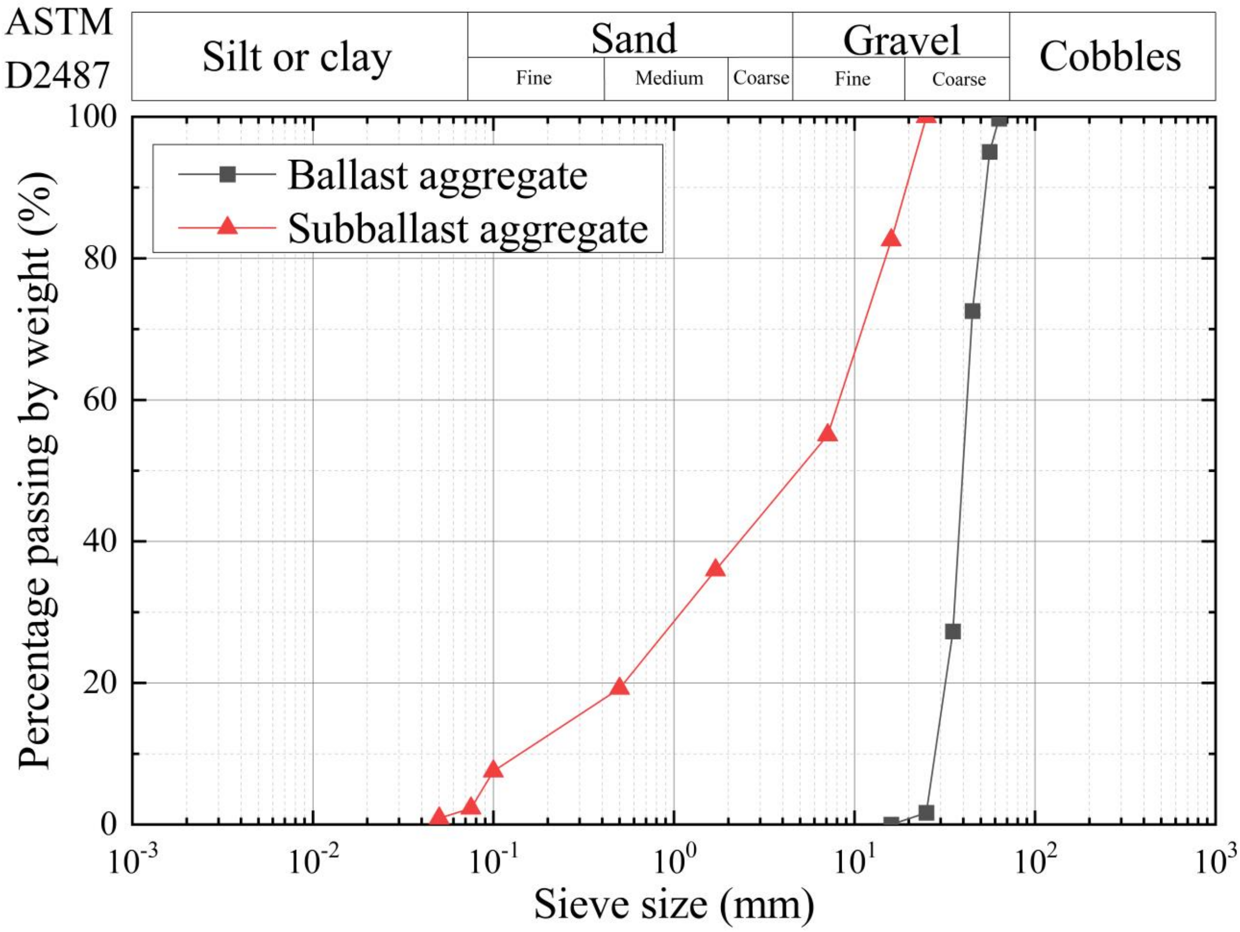

Figure 2. Particle size distribution of geo-materials used in the test.

Table 1. Properties of geo-materials used in the test.

Material	**Solid density** (kg/m^3)	**Packing density** (kg/m^3)	**K30 stiffness** *(MPa/m)*
Ballast	2613.8	1714.1	/
Subballast	/	2008.6	276-416
Subgrade	/	1931.1	216-280

Note: The minimum K30 values for subballast and subgrade are 190 MPa/m and 130 MPa/m according to the Chinese High-speed Railway Design Code (TB 10621-2014).

The dynamic train load applied to the trackbed was generated by the wheel-rail interaction and transmitted from the fastener system to the sleeper, which translates the moving train load into a fixed vibration load acting on the ballast layer. Fig. 3 schematically presents a train-rail-substructure dynamic interaction model [31], from which dynamic forces on railpads due to train passages at different speeds can be determined as the input load signals in the tests on the ZJU-iHSRT [8, 11]. Track irregularities could cause dynamic forces on railpads when the train runs at high speed [32-37], in this paper, the track irregularities generated from the Power Spectral Densities (PSD) of the sixth grade U.S. railway tracks were adopted in the aforementioned train-rail-substructure dynamic interaction model [38, 39]. The distributed sequential loading system of ZJU-iHSRT consists of the reaction frame, the loading frame, and eight hydraulic actuators located at equal intervals by fasteners. The input load acting on each fastener was calculated with the theoretical analysis model with the output train load that was reproduced in the above full-scale ballasted track through a distributed sequential loading system. During the loading process in a test, the output train loads were applied to the 50 cm long segmented rails using the loading frame through the hydraulic actuator with a time difference δ between the output loads, and then transferred to the sleepers and the ballast layers through the fastener system.

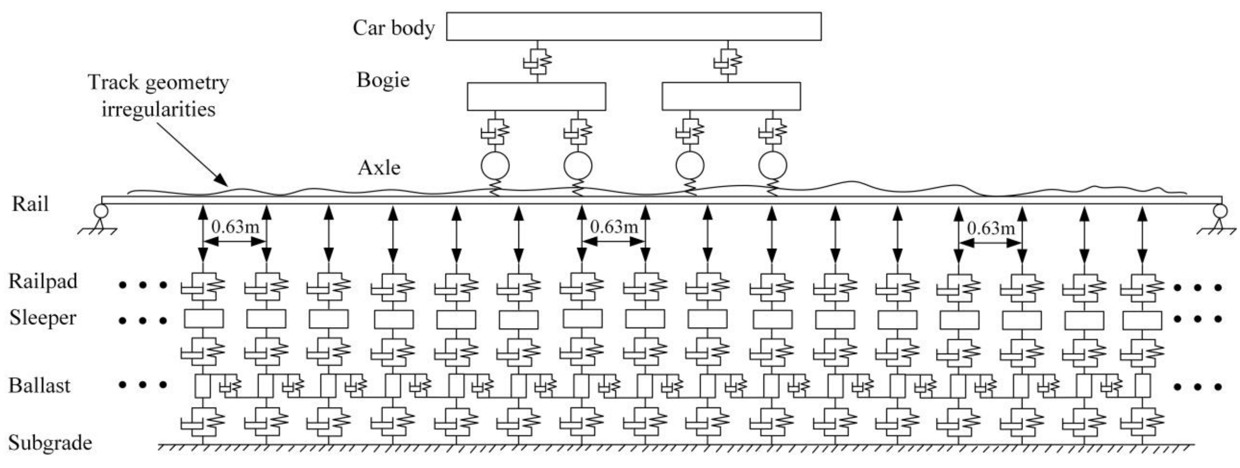

Figure 3. A train-rail-substructure dynamic interaction model for determining dynamic forces on railpads.

2.2. Instrumentation

The instrumentation, including the soil pressure sensors, laser displacement sensors, linear variable differential transformer (LVDT)-settlement plates, vibration velocity sensors, and “SmartRock” sensors (see Fig. 4), were calibrated and implemented after the construction of the ballasted track. As shown in Fig. 1 (a), eight soil pressure sensors were distributed on the subballast layer surface and subgrade surface to record the vertical soil stresses at different locations in the trackbed, and ten laser displacement sensors were placed on the sleeper edges to record the sleeper displacements. In order to record the cumulative deformations of the trackbed layers, sensors consisting of LVDTs and the settlement plate were placed on the subballast surface and subgrade surface. Eight vibration velocity sensors were set on the sleeper surface and the ballast bed, and ten wireless “SmartRock” sensors were embedded in the ballast bed to capture the particle-scale ballast movement characteristics.

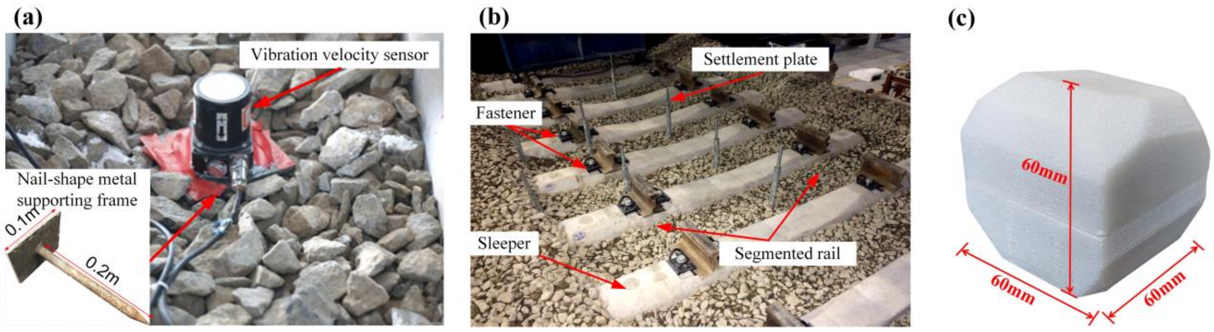

Figure 4. Instrumentation used in experiment: (a) vibration velocity sensor; (b) LVDT-settlement plate; (c) “SmartRock” sensor.

2.3. Experiment design

The experiment design contains three consecutive test phases as shown in Table 2. Phase 1 and Phase 3 are the very short dynamic response tests at four different train speeds and a 17-tonne axle load used to study the changes of ballasted track behavior before and after the application of the long-term train loading reported in this study. Phase 2 is the long-term train loading for the 500,000 train carriages in total to trace the track deformation and the associated stress, vibration and ballast degradation evolution. Phase 2 comprises of five loading stages with three different train speeds and axle load configurations which realistically captured both high-speed passenger and slow-moving freight train loads.

Table 2. Loading design of test phases

Test Phase	Loading stage	Train speed (km/h)	Axle load (tonne)	No. of train carriages	Wheel passes
1	1-4	100/200/300/360	17	25*4	100*4
2	1	100	17	100000	400000
	2	360	17	100000	400000
	3	360	17	100000	400000
	4	360	17	100000	400000
	5	100	25	100000	400000
3	1-4	100/200/300/360	17	25*4	100*4

Note: 1 train carriage = 4-wheel passes.

3. Results and discussions

3.1. Ballast degradation

The ballast degradation includes the deterioration of both the particle size and morphological characteristics. Different indexes and related definitions have been proposed for describing the morphological properties of aggregate particles since the 1930s [40-43]. The indexes of particle size mainly include the particle size distribution (PSD), volume/surface area and morphological characteristics including the form (flat and elongated ratio, sphericity, etc.), the angularity (roundness, angularity index), and the surface texture (surface texture index). In this study, the PSD was used to evaluate the particle size change, and the widely used flat and elongated ratio (FER), sphericity, convexity and angularity index were adopted to describe the deterioration of the particle morphological properties. This paper used a computer-aided particle morphology analyzing approach to trace the evolution of ballast particle morphology in a loading test [15, 25].

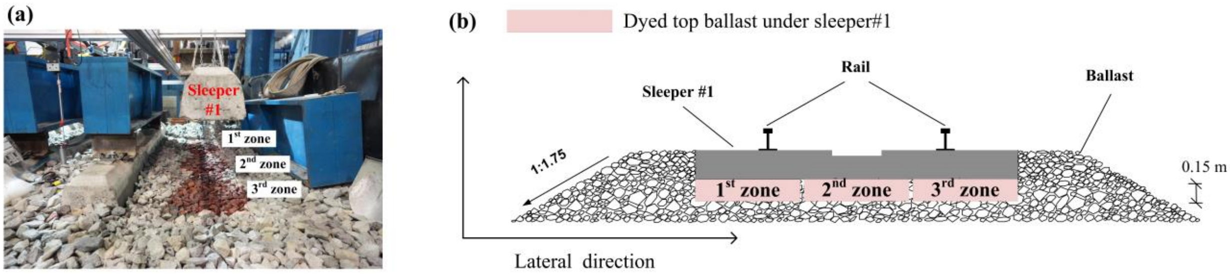

Figure 5. Morphological analysis of dyed top ballast under the sleeper: (a) dyed ballast under sleeper#1; (b) test layout of dyed ballast.

As shown in Fig. 5, a red non-oily dye was used to dye the top ballast particles underneath sleeper#1 in three 15 cm-deep zones, whereby the influence of the non-oily dye on the surface roughness and the internal friction angle was found to be negligible [44]. During the long-term train loading process in Phase 2, the dyed ballast in these three zones was sampled before the test and after every loading stage, and a sieving test and a ballast morphological analysis were performed using a verified ballast morphology imaging and analysis platform. The imaging platform consists of three high-precision industrial cameras with two sets of backlight boxes perpendicular to each other that are linked to a computer for data collection [25]. Ballast particle segmentation and reconstruction algorithms were developed for the three-camera device were used to capture the optical orthogonal views from imaging and for performing morphological analyses of the ballast particles. All three cameras are mounted on a bracket which can adjust the positions and angles of cameras precisely to ensure that they are orthogonal to each other and are equal distance from the target ballast particle on the desktop. They are connected to the computer with data cables. The ballast analysis system combines the algorithm for obtaining the mean surface and the boundary key points of a particle with the proven image processing methods in computer graphics. The basic ballast particle shape analysis process of this system is divided into three main parts [25]: (1) image recognition and segmentation, (2) outline extraction and simplification, and (3) morphological property index or parameter calculation.

The photos of fresh and degraded ballast particles after 500,000 train carriages are shown in Fig. 6. All three zones under the sleeper experienced considerable particle breakage as many small particles with a diameter below 25 mm were created after 500,000 train loading carriages. It was also obvious that the coloured dye on the ballast particle surfaces all significantly faded due to the serious ballast abrasion.

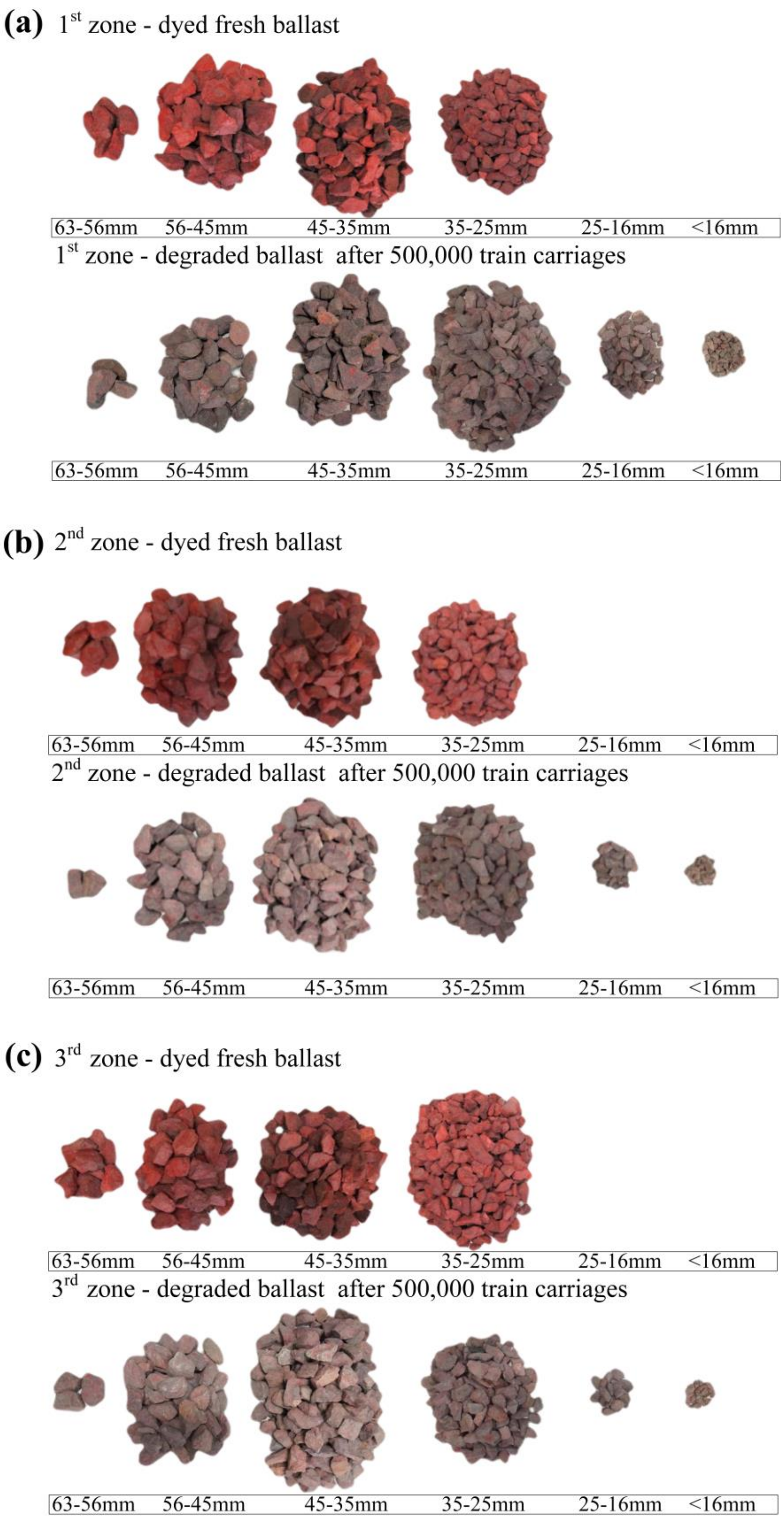

Figure 6. Comparison of dyed fresh ballast and degraded ballast after 500,000 train loading carriages: (a) 1st zone; (b) 2nd zone; (c) 3rd zone.

Particle size distribution and BBI

Fig. 7 shows the PSD curves of the dyed ballast obtained from the sieving tests. All three sample zones suffered the effects of particle breakage as shown by the shifts in the PSD curve. The passing percentages by mass of ballast particles with the large diameter sizes of 63–45 mm in the three zones decreased by 8.32 %, 13.58 %, and 16.97 %, while the percentages of small particles with diameter sizes less than 25 mm increased to 10.74 %, 11.42 %, and 10.84 %, respectively, which showed that the long-term train load caused the ballast particles under the sleepers to be significantly crushed into smaller particles.

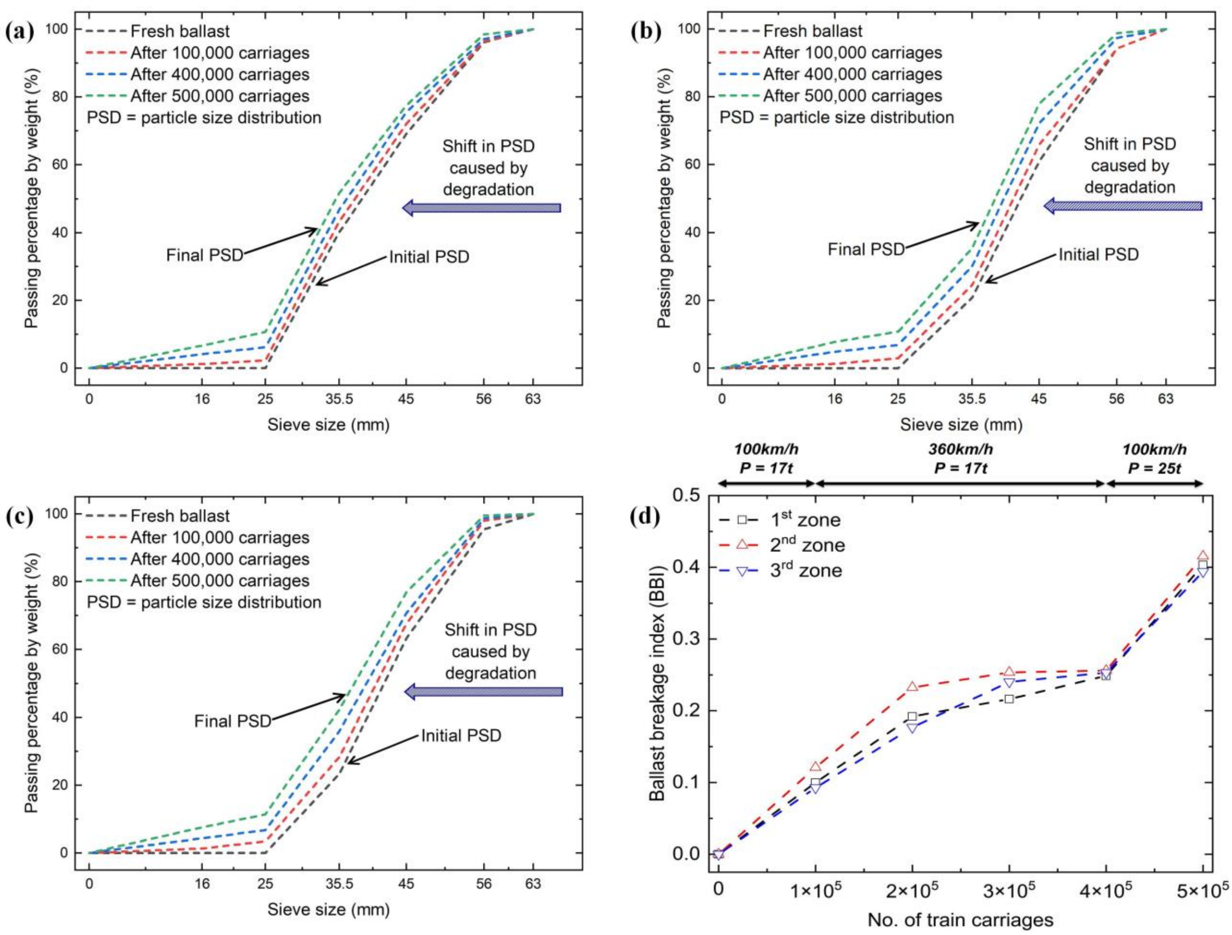

Figure 7. Evolution of PSD and ballast breakage index (BBI) of dyed ballast under the sleeper #1: (a) PSD in 1st zone; (b) PSD in 2nd zone; (c) PSD in 3rd zone; (d) ballast breakage index.

The ballast breakage index (BBI) proposed by Indraratna [18] is also adopted to quantify the ballast breakage in this paper, as shown in Fig. 7 (d).

$$BBI = \frac{A}{A + B} \quad (1)$$

A = shift in particle size distribution curve traces caused by degradation; and B = potential breakage or area between arbitrary boundary of maximum breakage and final particle-size distribution. The smallest particle size used in the calculation was 0 mm rather than the smallest sieve size 16 mm, because the smallest sieve size recommended by the Chinese standard is too large to consider for the newly generated small particles caused by ballast degradation. In this test, the BBI of these three zones were around 0.1 after the first 100,000 train loading carriages, and the BBI continued to increase when the loading train speed increased to 360 km/h in the next 100,000 train loading carriages which agrees well with previous laboratory investigations related to the effect of loading frequency [45, 46]. It's observed that the growth rate and the increment of the BBI in the 2nd zone were slightly larger than those of the other zones, one possible explanation is that stronger confinement of ballast particles in 2nd zone would cause more severe ballast breakage and corresponding larger BBI [18-21]. Also, the dynamic stresses in ballast layer right beneath railpads are highest and may cause most ballast breakage, but it's noted that 1st zone and 3rd zone also include the ballast particles beneath the sleeper edges where dynamic stresses are low (as shown in Fig. 11), so the average ballast breakages may become smaller, and BBI is smaller correspondingly. During the next 200,000 train loading carriages, the BBI values of all these three zones stabilized since there were no changes in the train speed or the axle load. When the axle load was increased to 25 tonnes in the final 100,000 train loading carriages, the BBI of all three zones increased sharply by over 50 % to around 0.35, because the increased impact energy of the larger axle load led to increased stresses in the trackbed which caused more severe ballast breakages [19, 47, 48].

Morphology properties

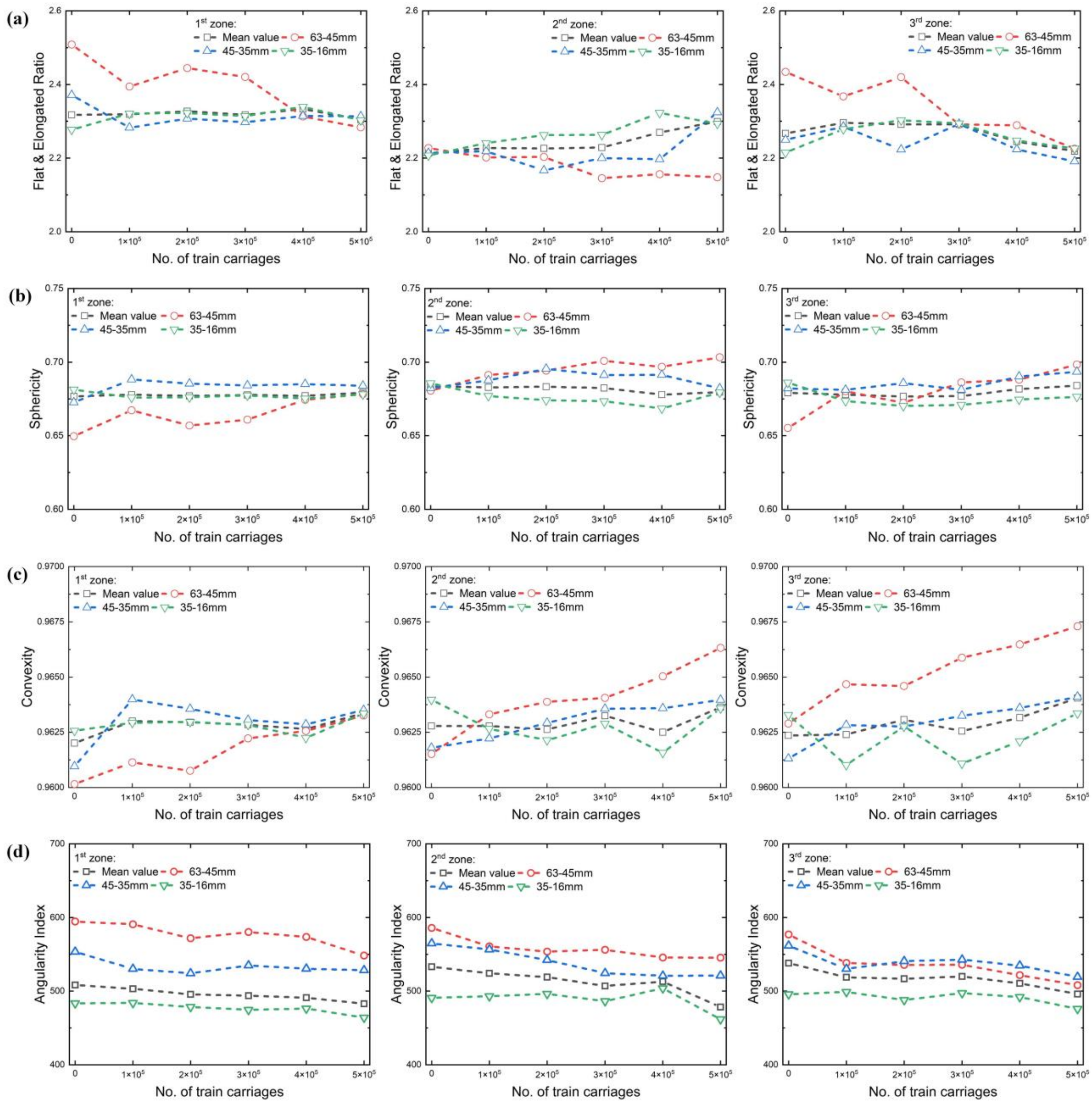

Figure 8. Changes of morphological characteristics of dyed ballast under long-term train loads: (a) flat & elongated ratio; (b) sphericity; (c) convexity; (d) angularity index.

Since the dyed ballast particles with a diameter of less than 16 mm in the test were all produced from the breakage of large ballast particles and hard to sample during the test, the new broken small particles with a diameter of 16 mm or less were not taken into the computer-aided ballast shape analysis in the test. Fig.8 presents the statistical mean values of ballast morphology properties for three different diameter ranges, and mean values of all the ballast particles in each zone are also given to describe the overall tendency. The FER quantifies the ratio of the longest to the shortest dimensions of a particle in an assembly of flat, elongated, cubical particles [49], as shown in Fig. 8 (a). The FER of these three large-diameter zones (63-45 mm) was reduced obviously, showing that the large ballast particles were prone to bear abrasion and particle breakage, which agreed with the previous triaxial test results [50, 51]. The lower FER means severe fracture and the sharp corner abrasion of the large particles occurred in the test, meaning that there were fewer slender and flaky particles after the long-term train loads. The FER of the ballast particles with a medium and small diameter (45–35 mm and 35-16 mm) fluctuated slightly and was stable. The sphericity quantifies the cube root of the ratio of the volume of the particle to the volume of its circumscribing sphere [52], as shown in Fig. 8 (b). The large diameter ballast particles (63-45 mm) experienced a slight increase in terms of the sphericity value, indicating that the shape of large ballast particles became more compact after the test. Moreover, the sphericity of the ballast particles with a medium and small diameter (45–35 mm and 35-16 mm) also fluctuated slightly and was stable compared with the large particles. The convexity quantifies the ratio of the area to the convex area from the two-dimensional projection of particle [53], as shown in Fig. 8 (c), presented a slowly increasing trend, and the amount of large ballast particles (63-45 mm) increased. The protruding edges and corners of the large particles were easier to break in the test, and the concave part of the outer surface gradually decreased. This trend was more obvious than that of the smaller particles. The angularity index quantifies the total changes in the angle of vertexes inscribed in a two-dimensional (2D) image silhouette outline influenced by corners and sharp versus smooth edges of a particle [54], as shown in Fig. 8 (d). With the increase of the number of loading train carriages, the angularity index of ballast particles within all three diameter range all gradually decreased, meaning that the angularity of ballast particles decreased and the particle boundaries became smoother under the long-term train loads.

Ballast shape class

The ballast particles could be divided into ten different shape classes according to the Sneed and Folk form triangle [55]: (1) Compact (C), (2) Compact-Platy (CP), (3) Compact-Bladed (CB), (4) Compact-Elongate (CE), (5) Platy (P); (6) Bladed (B), (7) Elongate (E), (8) Very-Platy (VP), (9) Very-Bladed (VB), and (10) Very-Elongate (VE). The ballast particle shape information (the largest size L, the median size I, and the smallest size S) obtained through the ballast morphology imaging and analysis platform as shown in Fig. 5 (c) was used to classify the shape classes of the ballast particles (see Fig. 9), and the value of sphericity was also included in the form triangle. More than 90% of the ballast particles within all the three diameter ranges were located in the middle six shape classes (CP, CB, CE, P, B, and E) in the form triangle, which meant that most of the ballast particles had a comparatively stable shape rather than VP, VB, and VE. As shown in Table 3, the proportions of whole ballast particles located on the top four shape classes (C, CP, CB, and CE) for all diameter ranges increased from 32.5 % to 35.2 %, as the overall particle shape class became more compact after 500,000 train loading carriages. Moreover, the proportions of large diameter (63-45 mm), medium diameter (45-35 mm) and small diameter (35-16 mm) ballast particles located on the bottom six shape classes (P, B, E, VP, VB and VE) with decreased from 75.1 %, 64.2 % and 59.3 % to 69.2 %, 63.6 % and 59.6 %, respectively, demonstrating that larger ballast particles of more Platy, Bladed and Elongate shapes suffered great degradation. The number of large and medium ballast particles located in the bottom three shape classes (VP, VB, and VE) were obviously reduced by comparing the triangles of fresh ballast and ballast after 500,000 train loading carriages. But the number of small-diameter particles of almost all the shape classes significantly increased after the long-term train loading because of the severe particle breakage, as shown in Fig. 9 (c).

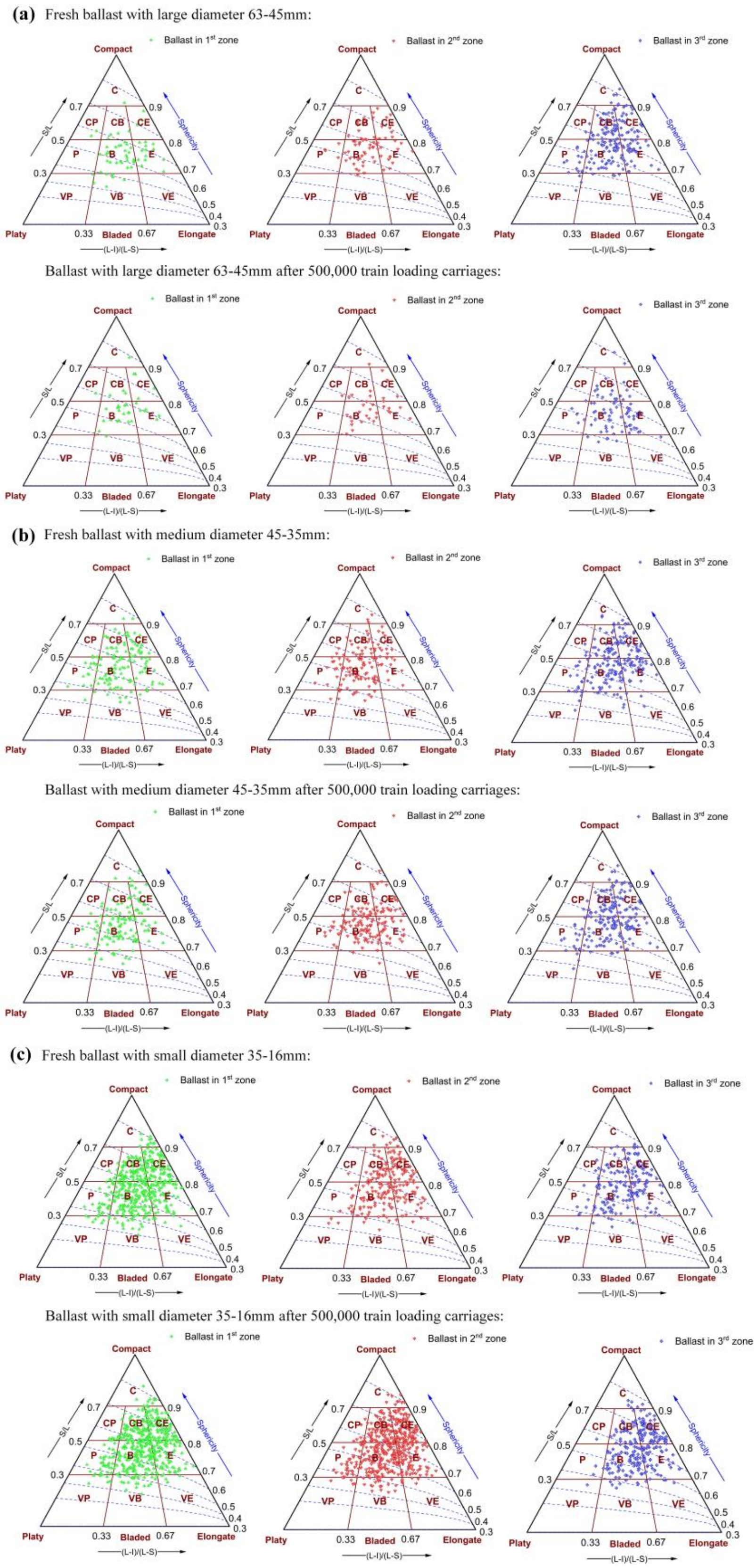

Figure 9. Changes of ballast particle shape classes under long-term train loads: (a) large diameter 63-45 mm; (b) medium diameter 45-35 mm; (c) small diameter 35-16 mm.

Table 3. Particle number of different shape classes with all particle size range.

Ballast Shape chass	Particle Number of all three zones					
	New constructed track			After 500,000 train carriages		
	large diameter (63-45 mm)	Medium diameter (45-35 mm)	Small diameter (35-16 mm)	large diameter (63-45 mm)	Medium diameter (45-35 mm)	Small diameter 35-16 mm)
C	3	12	22	4	13	25
CP	3	6	12	3	10	18
CB	25	74	132	16	75	176
CE	21	85	177	13	62	233
P	8	44	47	5	37	66
B	83	167	260	48	159	319
E	52	82	140	21	57	205
VP	1	4	11	0	5	13
VB	12	16	34	7	22	53
VE	1	5	8	0	0	10
Total	209	495	843	117	440	1118

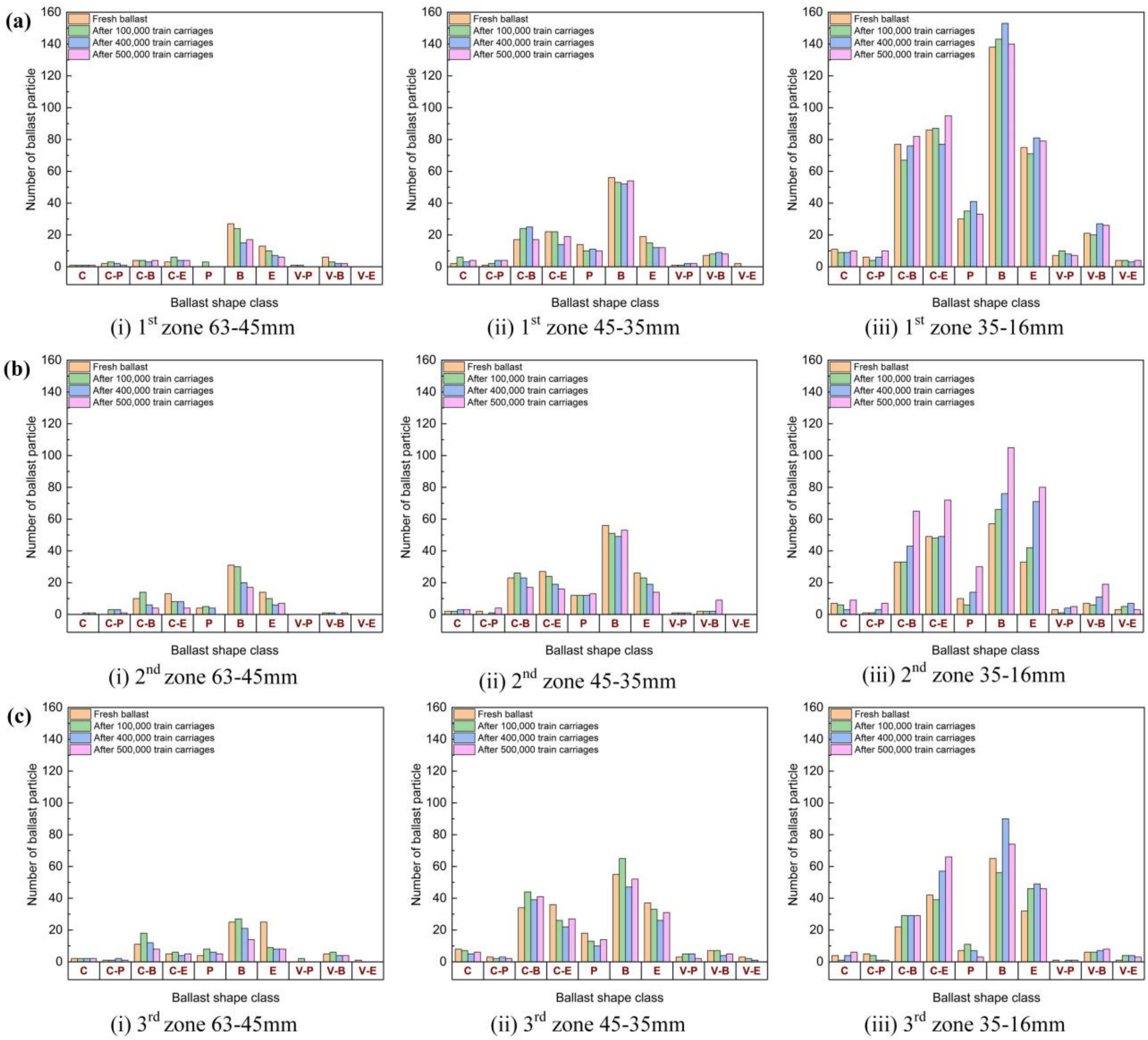

Figure 10. Ballast particle number of different shape classes under long-term train loads.

According to the number of ballast particles distributed in the Folk form triangle, the ballast particle number of different shape classes in all three zones under the sleeper could be sorted out at each loading stage, as shown in Fig. 10. The number of large-diameter ballast particles (63–45 mm) in the three different zones all decreased during the long-term loading progress, while the number of small-diameter ballast particles (35–16 mm) almost all increased as the ballast particles with large diameters experienced breakage. The number of large-diameter particles (63–45 mm) for specific shape classes (Platy, Bladed, Elongate) in all three zones gradually dropped, showing that the large ballast particles with a relatively large FER and small sphericity were easier to degrade according to the coordinates in the Folk form triangle, and related tests obtained similar conclusions [56]. The number of small ballast particles between 35 and 16 mm in the 2nd zone increased sharply for almost all shape classes during the final loading stage, showing that the increase in the axle load could cause more serious particle breakage and shape class change in the middle zone under the sleeper.

3.2. Dynamic soil stress on subballast and subgrade surface

The discontinuous nature of the subgrade materials can lead to a non-uniform stress distribution in the trackbed, which has been widely considered to be following the pyramidal load pattern [57]. The existing research on the stress distribution pattern in the trackbed has mainly focused on the sleeper-ballast interface, and both field measurements and the theoretical analysis results have shown that the contact stress between the sleeper bottom and the ballast layer followed a hyperbolic distribution pattern that achieved the peak value under the rail seat [58-60]. In this section, the dynamic stress responses measured at selected locations within the trackbed are presented for four different train speeds.

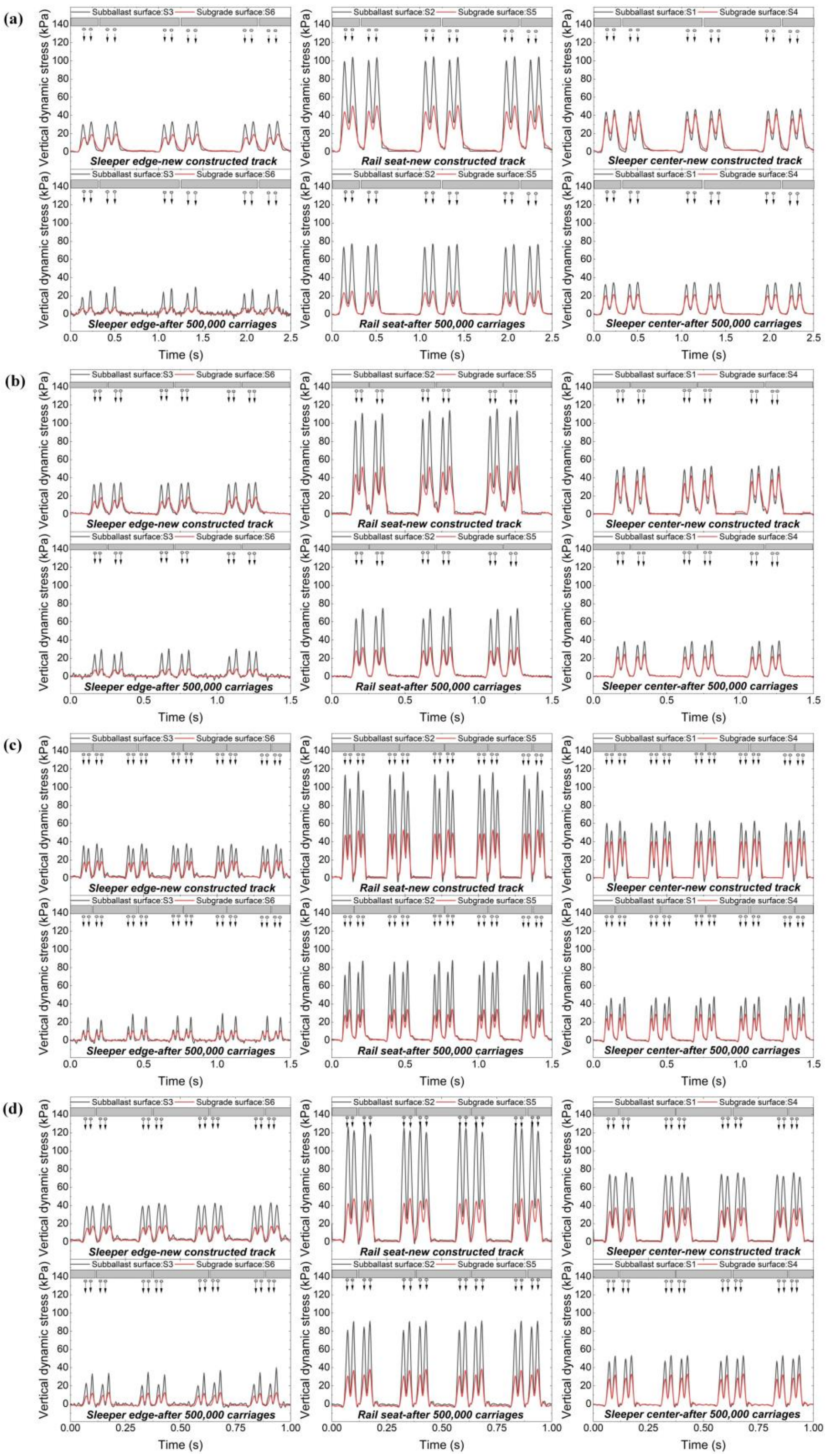

Figure 11. Comparasion of dynamic soil stresses at different locations under the sleeper: (a) 100 km/h-17 tonne; (b) 200 km/h-17 tonne; (c) 300 km/h-17 tonne; (d) 360 km/h-17 tonne.

Fig. 11 shows the time histories of the vertical dynamic stresses measured by the soil pressure sensors for four train speeds (see Table 2 for Phase 1/3 information) before and after the action of 500,000 train loading carriages. The locations of these sensors are summarized in Fig. 1, with S1, S2, and S3 on the subballast top surface, while S4, S5, and S6 on the subgrade top surface. The vertical dynamic soil stresses experienced significant attenuation during the transmission process from the subballast surface to the subgrade surface – this can be clearly seen when comparing the pairs of measurements S1/S4, S2/S5, S3/S6. The dynamic stress amplitude of each location increased slightly with the increase of the train speed, which was consistent with previous test results [11]. The vertical stress amplitudes under the rail seat (S2/S5) were significantly higher than those for the locations under the sleeper edge (S3/S6) and the sleeper center (S1/S4) since this was where the train load was applied. This is also in line with previous observation that the area between the sleeper and the ballast layer under the rail seat always has more effective contact status, which was conducive to the transmission of dynamic stress [61, 62]. By comparing the dynamic soil stresses before and after 500,000 train loading carriages shown in Fig. 11, it was found that the dynamic soil stress amplitudes of different locations at both subballast surface and the subgrade surface decreased significantly, and the drops at locations (S2/S5) under the rail seat were the most significant. The vertical dynamic soil stress amplitude peaked at the locations under the rail seat with the S2 sensor at the bottom of the ballast layer measuring 100.2 kPa, 104.1 kPa, 117.2 kPa, and 127.7 kPa in Phase 1 and 74.9 kPa, 76.6 kPa, 87.8 kPa, and 91.3 kPa in Phase 3 at the train speeds of 100 km/h, 200 km/h, 300 km/h, and 360 km/h respectively. These correspond to dynamic stress reductions of 25 %, 26 %, 25 %, and 28 %, respectively. The results show that the application of the long-term train loads densified the trackbed and enhanced the contact status between the sleeper and the trackbed, which results in a more than 25% reduction in the peak dynamic stress compared to when it was new. It appears that the particle rearrangement and particle breakage provided by 500,000 train loading carriages made the trackbed better at dissipating the dynamic stresses especially in the highly stressed zones under the rail seat.

3.3. Vibration of sleeper and ballast bed

Vibration velocity of sleeper and ballast bed

Fig. 12 shows the time histories of the vibration velocities (see Table 2 for Phase 1/3 information) at different locations of the sleeper surface and the ballast bed before and after the application of 500,000 train carriage loadings. Sensors V2, V3, and V4 were on the surface of the crib ballast which between the sleepers, V5 and V6 were attached to the center and the edge of sleeper#4's surface, and V7 and V8 were set at the surface and the edge of the shoulder ballast. The vibration velocities measured on the sleeper surface (center-V5 and edge-V6) for different loading stages were always higher than those measured on the crib ballast and the shoulder ballast because the vibration caused by the quasi-static axle load excitation and the dynamic excitation of the wheel-rail contact underwent a significant decline during the transmission from the sleeper to the ballast bed [63]. The vibration velocities at different locations all surged with the increase of the train speed in both Phase 1 and 3. But the vibration velocity amplitudes after the action of 500,000 train loading carriages all decreased tremendously compared with the new constructed track. The vibration velocity amplitudes on the crib ballast peak at V3 around the rail seat and at V3 were 3.65 mm/s, 11.2 mm/s, 18.25 mm/s, and 19.3 mm/s in Phase 1 and 2.25 mm/s, 5.52 mm/s, 10.57 mm/s, and 11.83 mm/s in Phase 3 at the train speeds of 100 km/h, 200 km/h, 300 km/h, and 360 km/h, which were decreased by 38.36%, 50.71%, 42.08%, and 38.7%, respectively. This reduction in vibration velocity showed on the ballast bed suggests that the ballast bed became more stable with increased ballast breakage and trackbed settlement. The long-term train loads densified the trackbed, and particle rearrangement and particle breakage made the small particles fill the ballast voids then vibration became better to transmit and dissipate, reducing the vibration of sleeper and ballast bed.

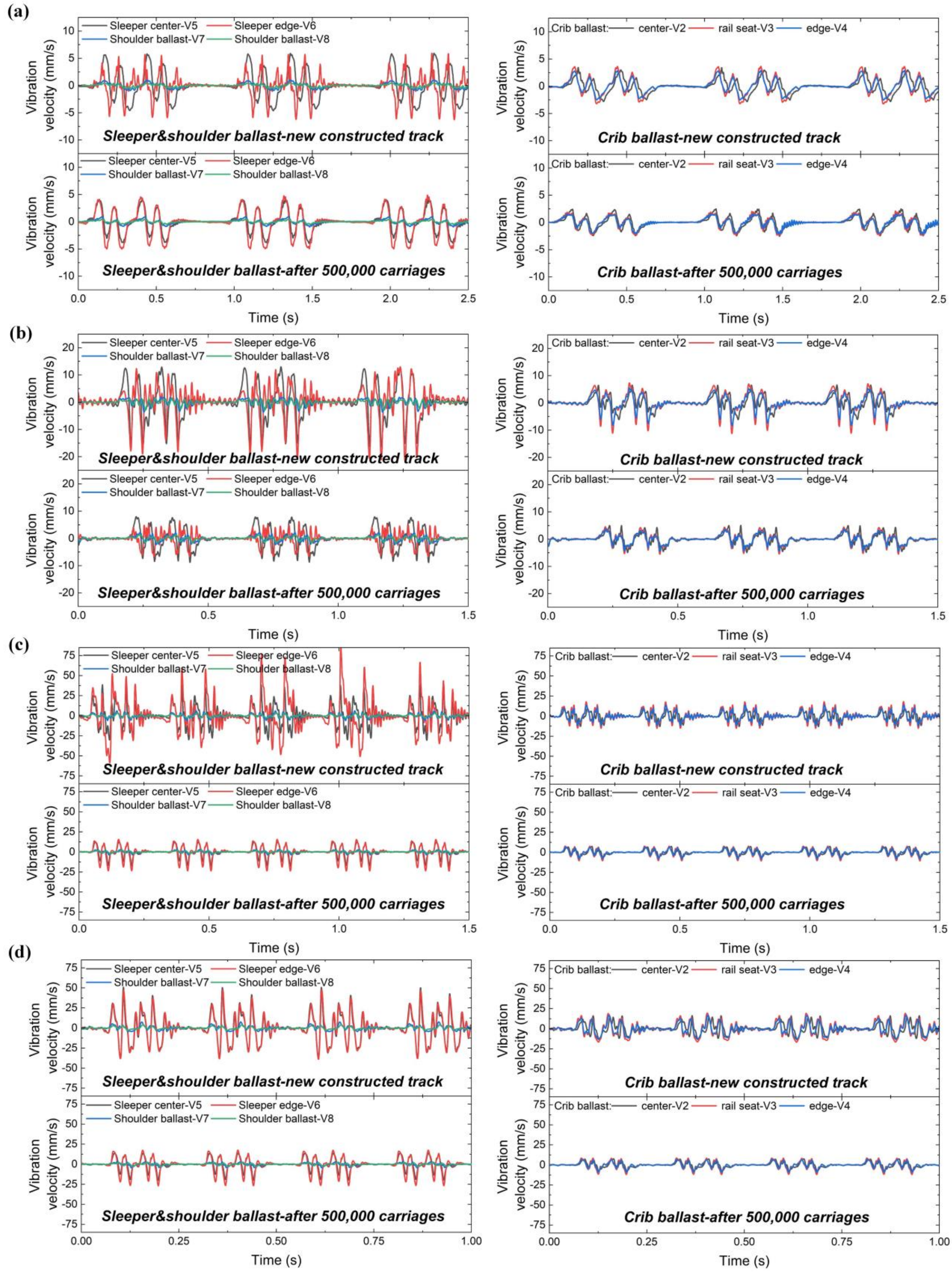

Figure 12. Comparison of vibration velocities between the new constructed track and after 500,000 train carriages on the sleeper and ballast bed (axle load = 17 tonnes): (a) 100 km/h; (b) 200 km/h; (c) 300 km/h; (d) 360 km/h.

Translational acceleration of "SmartRock" in ballast bed

As shown in Fig. 1 (a), the "SmartRock" sensors were buried in the ballast bed under sleeper #4. R8, R9, and R10 were carefully placed at the top of the ballast bed directly underneath the sleeper bottom, while R1, R2, and R3 were located on the surface of the bottom ballast which in the middle depth of the ballast bed, and R4 and R6 were located in the ballast shoulder. Fig. 13 presents the time histories of the vibration accelerations recorded by R8, R9, R10, and R6. These SmartRocks vibrated in the lateral, longitudinal, and vertical directions as the vibration propagated through the contacts between adjacent ballast particles in the ballast bed. As shown in this figure, the acceleration amplitude of R6 at the ballast shoulder was much smaller than those of the other SmartRocks at the same depth, which showed the vibration experienced significant attenuation in the transmission process from the sleeper to the ballast bed shoulder. The translational acceleration amplitudes peaked at R9 underneath the rail seat, and decayed laterally because this zone below the rail seat had more effective contacts and it made the vibration easier to spread through particle contacts [64]. The amplitudes of the particle accelerations under the sleeper (R8, R9 and R10) in all three directions increased by over eight times when the train speed increased from 100 km/h to 300 km/h in the new constructed track (Phase 1), which highlights that ballast particle movements are significantly activated by the increase of train speed. Furthermore, the amplitudes of the particle accelerations under the sleeper (R8, R9 and R10) in lateral and longitudinal directions were significantly higher than the vertical direction when the train speed is higher than 100 km/h, which indicates that the high-speed train load accelerated ballast particles flow away from the sleeper in both lateral and longitudinal directions with the squeezing effect of the vertical dynamic load. Additionally, all the acceleration amplitudes declined after 500,000 train loading carriages, which suggests that the ballast particle movements decreased and the inside ballast bed became more stable with the increased BBI and settlement. The long-term train loads densified the ballast bed, and ballast movement and particle breakage made ballast voids filled then vibrations became better to transmit and dissipate, reducing the particle acceleration in the ballast bed.

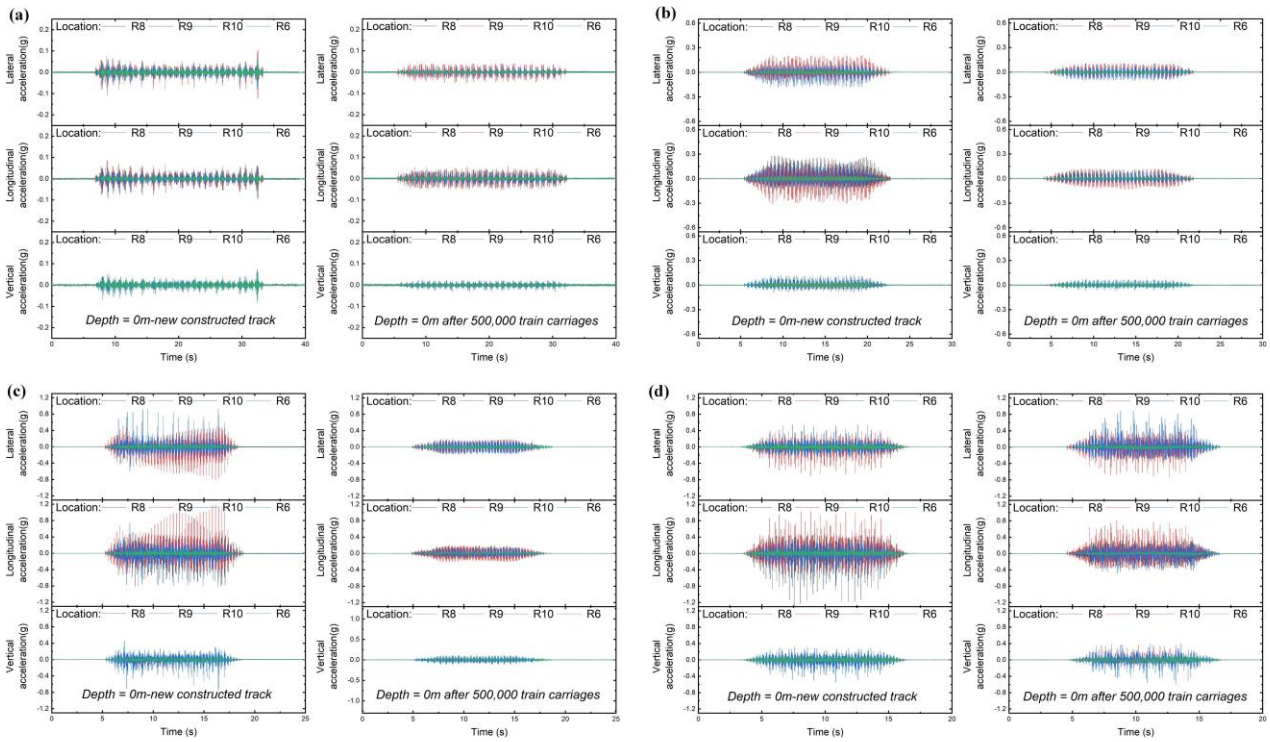

Figure 13. Comparison of translational accelerations between the new constructed track and after 500,000 train carriages inside the ballast bed (axle load = 17 tonnes): (a) 100 km/h; (b) 200 km/h; (c) 300 km/h; (d) 360 km/h.

3.4. Accumulated settlement of trackbed

The vertical deformation of the trackbed layers under repeated train traffic loads is mainly caused by the particle rearrangement to a denser packing, and ballast particle breakage with the smaller particles moving into the voids of the larger particles [65]. Fig. 14 shows the long-term settlements of the trackbed measured by the laser displacement sensors under the moving train loads of 500,000 train carriages in Phase 2.

As shown in Fig. 14 (a), the accumulated settlement of each sleeper developed relatively slowly at a train speed of 100 km/h for the initial 100,000 train loading carriages. The development of the accumulated settlements of sleepers #3-6 sped up while other sleepers near the boundaries had a lower increment during the second 100,000 train loading carriages at a higher speed of 360 km/h. It can be noted that the accumulated settlements of the central sleepers #3-6 were always larger than the others throughout the loading stages [Fig. 14 (b)] because the trackbed were constrained by proximity to the end boundaries with the metal box, resulting in smaller trackbed deformation.

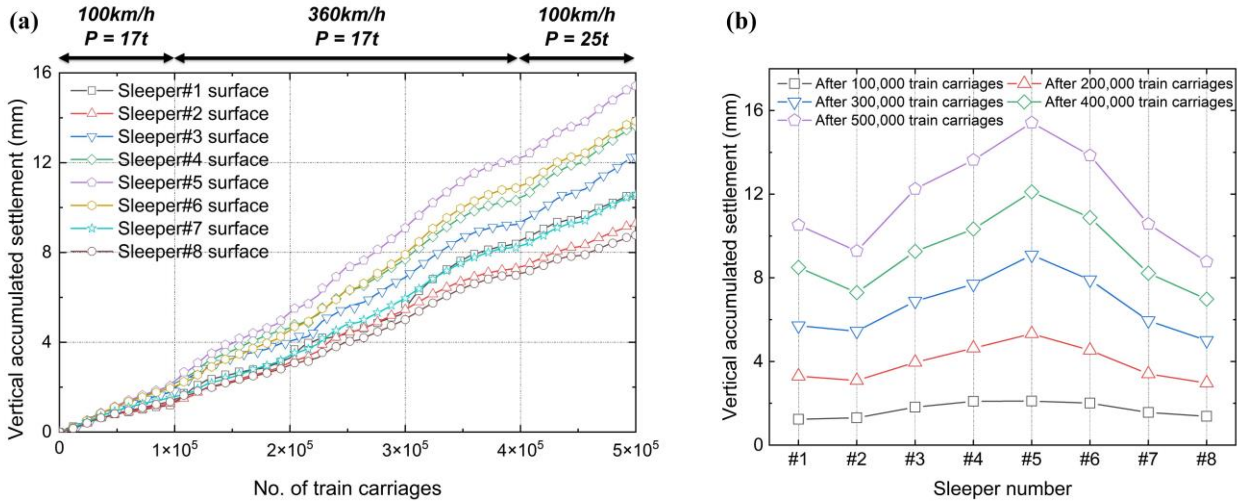

Figure 14. Long-term settlement of sleepers during 500,000 train carriages: (a) vertical settlement at sleeper surfaces; (b) accumulated settlement after each loading stage of Phase 2.

The particle rearrangement contributed to the surging of the accumulated settlements of the central sleepers (#3-6) in the second 100,000 train loading carriages considering the slopes of BBI curves nearly kept constant in Fig. 7 (d). The vibration accompanying the high-speed train load increased the trackbed settlement with its influence on particle rearrangement and lateral flow of the ballast. The rate of settlement in all the sleepers slowed significantly as the total train loading carriages approached 400,000. This is associated with the particle breakage slowing down and a reduction in the stresses and vibrations in the trackbed. In the final 100,000 train loading carriages when the axle load was increased to 25 tonnes, the accumulated settlements increased sharply again as the increased axle load caused a greater particle breakage and contributed to a greater deformation, even though the train speed was decreased to 100 km/h. It should be noted that the slightly higher accumulated settlement of sleeper #1 compared to the sleepers near the boundaries is because of the disturbance introduced in the excavating and sampling action of dyed ballast under sleeper #1 to study the ballast degradation evolution [see Fig. 14 (b)].

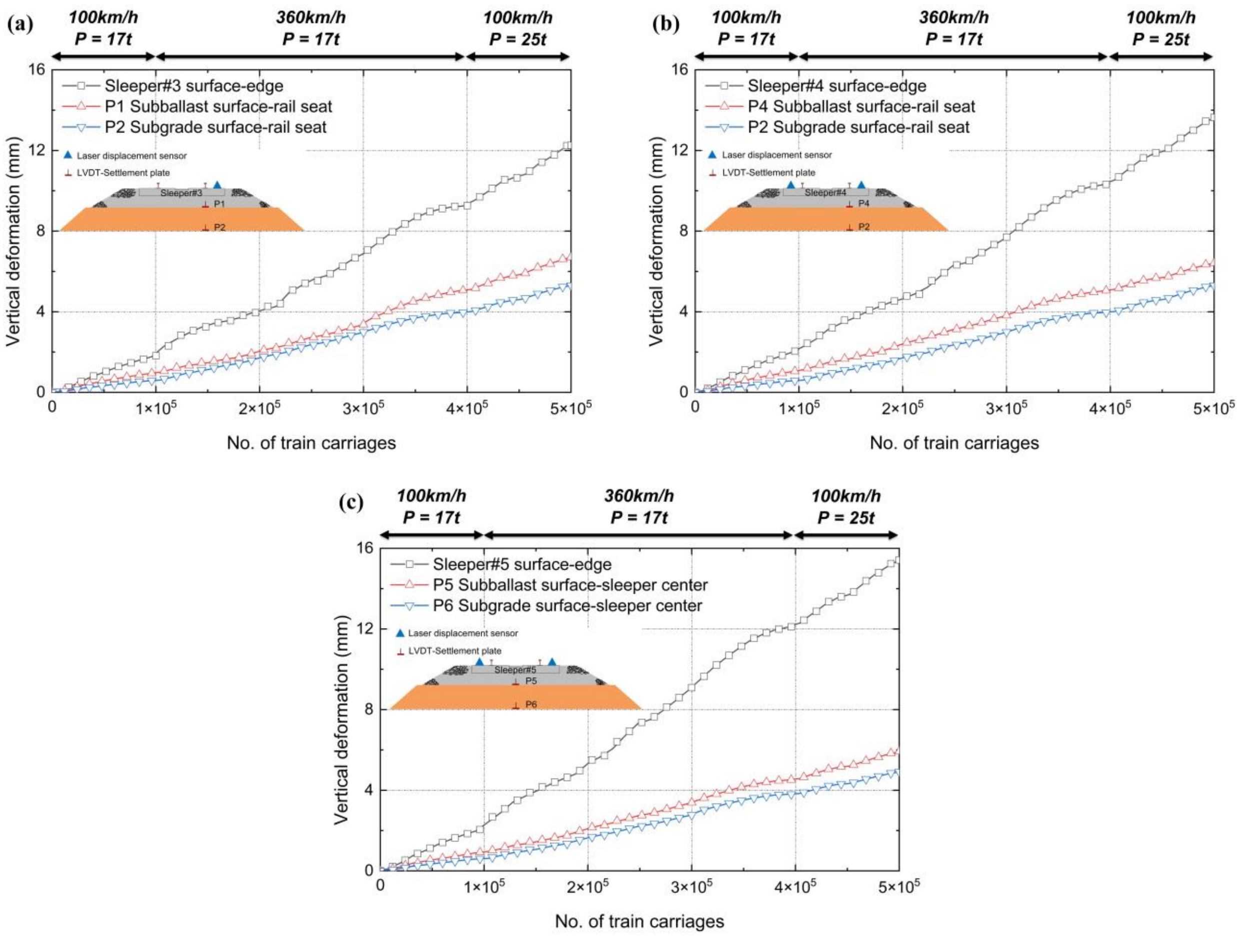

Figure 15. Vertical deformation of trackbed layers: (a) cross-section under sleeper #3; (b) cross-section under sleeper #4; (c) cross-section under sleeper #5.

The contributions to the total trackbed settlement from the trackbed layers can be seen in Fig. 15 which compares the sleeper/ground settlement with the vertical deformations measured at the the subballast top surface and the subgrade top surface under the central sleepers #3–5. The results show that over 50% of the long-term accumulated settlement came from the ballast layer of 0.30m thick. The settlement contribution from the 0.70m thick subballast layer under all three sleepers were much lower because the subballast material composed of fine-grained soil and gravel was compacted to a higher density (see Table 1). The 2.05 m thick subgrade layer also contributed significantly to the overall ground settlement under the long-term train loading.

4. Conclusions

This paper has presented an experimental study based on a full-scale physical model test platform (ZJU-iHSRT) and a computer-aided ballast shape analysis with the objective of investigating the ballasted track settlement associated with ballast degradation under a long-term train passages. From the test results, the following conclusions could be drawn.

(a) In the test, the long-term train loads caused significant ballast degradation in both the particle size and the morphology properties, and the ballast particles in the middle zone produced more severe ballast breakage which could be due to the stronger confinement in the mid-span under the sleeper. The overall ballast shape class became more compact after the test, and ballast particles with larger diameter and specific shape classes (Platy, Bladed, Elongate) were more likely to degrade.

(b) The vertical dynamic soil stresses and vibrations in the trackbed all peaked at the locations underneath the rail seat and decayed with the increase of the distance away from the rail seat. The long-term train loads densified the ballast bed, and particle rearrangement and particle breakage made ballast voids been filled, then stresses and vibrations became better to transmit and dissipate, making the trackbed more stable. The amplitudes of the vertical soil stresses and the vibration velocities around the rail seat in the trackbed were reduced by over 25% and 38%, respectively, after 500,000 train loading carriages.

(c) The increase of the train speed from 100 km/h to 300 km/h intensified the vibration acceleration amplitudes of the ballast particles under the sleeper by over eight times and caused intense ballast movement away from the sleeper in the lateral and longitudinal directions.

(d) The ballast trackbed experienced severe particle breakage in the test, and the ballast breakage index (BBI) rose dramatically by over 50% when the axle load increased from 17 tonnes to 25 tonnes in the last 100,000 train loading carriages, while the number of small particles increased sharply in the middle zone under the sleeper.

(e) Over 50% of the permanent accumulated settlement of the ballasted track resulted from the ballast bed deformation, and the increase in the train speed caused intense particle rearrangement in the ballast bed and accelerated the development of the accumulated deformation, while the increase in the axle load caused serious particle breakage and contributed to a greater deformation.

Credit authorship contribution statement

Qiusheng Gu: Experiment, Analysis, Writing.
Chuang zhao: Methodology, Review, Editing.
Xuecheng Bian: Methodology, Review, Funding acquisition.
John Paul Morrissey: Methodology, Investigation, Review.
Jin Yeam Ooi: Conceptualization, Resources, Review.

Declaration of competing interest

The authors declare that they have no known competing financial interests or personal relationships that could have appeared to influence the work reported in this paper.

Acknowledgement

Project supported by the Basic Science Center Program for Multiphase Evolution in Hyper-gravity at the National Natural Science Foundation of China (No. 51988101), the National Natural Science Foundation of China (No. 52008369) and the National Key Research and Development Program (No. 2018YFE0207100). The authors would also like to address their deep thanks to the support from China Scholarship Council (CSC).

References

[1] X.C. Bian, H.G. Jiang, Y.M. Chen, Accumulative deformation in railway track induced by high-speed traffic loading of the trains, Earthquake Engineering and Engineering Vibration, 9 (2010) 319-326.

[2] Q.D. Sun, B. Indraratna, S. Nimbalkar, Effect of cyclic loading frequency on the permanent deformation and degradation of railway ballast, Geotechnique, 64 (2014) 746-751.

[3] Q.D. Sun, B. Indraratna, S. Nimbalkar, Deformation and degradation mechanisms of railway ballast under high frequency cyclic loading, Journal of Geotechnical and Geoenvironmental Engineering, 142 (2016).

[4] Q.D. Sun, B. Indraratna, N.T. Ngo, Effect of increase in load and frequency on the resilience of railway ballast, Geotechnique, 69 (2019) 833-840.

[5] P.K. Thakur, J.S. Vinod, B. Indraratna, Effect of confining pressure and frequency on the deformation of ballast, Geotechnique, 63 (2013) 786-790.

[6] J. Eisenmann, G. Leykauf, L. Mattner, Recent development in German railway track design, Proceedings of The Institution of Civil Engineers-Transport, 105 (1994) 91-96.

[7] B. Indraratna, S. Nimbalkar, and C. Rujikiatkamjorn, Enhancement of rail track performance through utilisation of geosynthetic inclusions, Geotechnical Engineering Journal of the SEAGS & AGSSEA, 45 (2014) 17-27.

[8] X.C. Bian, H.G. Jiang, C. Cheng, Y.M. Chen, R.P. Chen, J.Q. Jiang, Full-scale model testing on a ballastless high-speed railway under simulated train moving loads, Soil Dynamics and Earthquake Engineering, 66 (2014) 368-384.

[9] H.G. Jiang, X.C. Bian, J.Q. Jiang, Y.M. Chen, Dynamic performance of high-speed railway formation with the rise of water table, Engineering Geology, 206 (2016) 18-32.

[10] X.C. Bian, H.G. Jiang, Y.M. Chen, J.Q. Jiang, J. Han, A full-scale physical model test apparatus for investigating the dynamic performance of the slab track system of a high-speed railway, Proceedings of the Institution of Mechanical Engineers Part F-Journal of Rail and Rapid Transit, 230 (2016) 554-571.

[11] W. Li, X.C. Bian, X. Duan, E. Tutumluer, Full-scale model testing on ballasted high-speed railway: dynamic responses and accumulated settlements, Transportation Research Record, 2672 (2018) 125-135.

[12] X.C. Bian, H. Huang, E. Tutumluer, Y. Gao, "Critical particle size" and ballast gradation studied by Discrete Element Modeling, Transportation Geotechnics, 6 (2016) 38-44.

[13] A.B. Göktepe, A. Sezer, Effect of particle shape on density and permeability of sands, Proceedings of the Institution of Civil Engineers - Geotechnical Engineering, 163 (2010) 307-320.

[14] P. Vangla, G.M.Latha, Influence of particle size on the friction and interfacial shear strength of sands of similar morphology, International Journal of Geosynthetics and Ground Engineering, 1 (2015) 6.

[15] X.C. Bian, W. Li, Y. Qian, E. Tutumluer, Micromechanical particle interactions in railway ballast through DEM simulations of direct shear tests, International Journal of Geomechanics, 19 (2019).

[16] G. Lees, C.K. Kennedy, Quality, Shape and degradation of aggregates, Quarterly Journal of Engineering Geology and Hydrogeology, 8 (1975) 193-209.

[17] J.C.O. Nielsen, E.G. Berggren, A. Hammar, F. Jansson, R. Bolmsvik, Degradation of railway track geometry - Correlation between track stiffness gradient and differential settlement, Proceedings of the Institution of Mechanical Engineers, Part F: Journal of Rail and Rapid Transit, 234 (2020) 108-119.

[18] B. Indraratna, J. Lackenby, D. Christie, Effect of confining pressure on the degradation of ballast under cyclic loading, Geotechnique, 55 (2005) 325-328.

[19] J. Lackenby, B. Indraratna, G. McDowell, D. Christie, Effect of confining pressure on ballast degradation and deformation under cyclic triaxial loading, Geotechnique, 57 (2007) 527-536.
[20] A. De Witt, K. Boston, B. Leshchinsky, Predicting aggregate degradation in forest roads in Northwest Oregon, Forests, 11 (2020).
[21] Y. Qian, E. Tutumluer, Y.M.A. Hashash, J. Ghaboussi, Effects of ballast degradation on permanent deformation behavior from large-scale triaxial tests, Proceedings of the ASME Joint Rail Conference, (2014).
[22] Y. Qian, E. Tutumluer, Y.M.A. Hashash, J. Ghaboussi, Effects of ballast degradation on shear strength behavior from large-scale triaxial tests, From Fundamentals to Applications in Geotechnics, (2015) 170-179.
[23] Y. Qian, D. Mishra, E. Tutumluer, Y.M.A. Hashash, J. Ghaboussi, Moisture effects on degraded ballast shear strength behavior, Proceedings of the ASME Joint Rail Conference, (2016).
[24] H.H. Huang, M. Moaveni, S. Schmidt, E. Tutumluer, J.M. Hart, Evaluation of railway ballast permeability using machine vision-based degradation analysis, Transportation Research Record, 2672 (2018) 62-73.
[25] X. Bian, K. Shi, W. Li, X. Luo, E. Tutumluer, Y. Chen, Quantification of railway ballast degradation by abrasion testing and computer-aided morphology analysis, Journal of Materials in Civil Engineering, 33 (2021).
[26] M. Moaveni, Y. Qian, I.I.A. Qamhia, E. Tutumluer, C. Basye, D. Li, Morphological characterization of railroad ballast degradation trends in the field and laboratory, Transportation Research Record, 2545 (2016) 89-99.
[27] S. Liu, H. Huang, T. Qiu, L. Gao, Comparison of laboratory testing using smartrock and discrete element modeling of ballast particle movement, Journal of Materials in Civil Engineering, 29 (2017) D6016001.
[28] S.S. Liu, H. Huang, T. Qiu, S.H. Shen, Sensing mechanism and real-time computing for granular materials, Journal of Computing in Civil Engineering, 32 (2018).
[29] S. Liu, T. Qiu, Y. Qian, H. Huang, E. Tutumluer, S. Shen, Simulations of large-scale triaxial shear tests on ballast aggregates using sensing mechanism and real-time (SMART) computing, Computers and Geotechnics, 110 (2019) 184-198.
[30] S. Liu, H. Huang, T. Qiu, B. Kerchof, Characterization of ballast particle movement at mud spot, Journal of Materials in Civil Engineering, 31 (2019).
[31] X.C. Bian, H.G. Jiang, C. Chang, J. Hu, Y.M. Chen, Track and ground vibrations generated by high-speed train running on ballastless railway with excitation of vertical track irregularities, Soil Dynamics and Earthquake Engineering, 76 (2015) 29-43.
[32] H. Takemiya, X.C. Bian, Substructure simulation of inhomogeneous track and layered ground dynamic interaction under train passage, Journal of Engineering Mechanics, 131 (2005) 699-711.
[33] J. Shi, W.-s. Fang, Y.-j. Wang, Y. Zhao, Measurements and analysis of track irregularities on high speed maglev lines, Journal of Zhejiang University SCIENCE A, 15 (2014) 385-394.
[34] X. Sheng, C.J.C. Jones, D.J. Thompson, A theoretical model for ground vibration from trains generated by vertical track irregularities, J Sound Vib, 272 (2004) 937-965.
[35] G. Lombaert, P. Galvín, S. François, G. Degrande, Quantification of uncertainty in the prediction of railway induced ground vibration due to the use of statistical track unevenness data, J Sound Vib, 333 (2014) 4232-4253.
[36] L. Xu, W. Zhai, A novel model for determining the amplitude-wavelength limits of track irregularities accompanied by a reliability assessment in railway vehicle-track dynamics, Mech Syst Signal Pr, 86 (2017) 260-277.
[37] X. Bian, W. Li, J. Hu, H. Liu, X. Duan, Y. Chen, Geodynamics of high-speed railway, Transportation Geotechnics, 17 (2018) 69-76.

[38] J. Hu, X. Duan, X. Bian, J. Jiang, Dynamic stresses in embankment and ground caused by HST with the considering of track irregularity, in: 7th International Symposium on Environmental Vibration and Transportation Geodynamics (ISEV), Hangzhou, PEOPLES R CHINA, 2016, pp. 233-242.
[39] X. Bian, C. Chao, W. Jin, Y. Chen, A 2.5D finite element approach for predicting ground vibrations generated by vertical track irregularities, J Zhejiang Univ-Sc A, 12 (2011) 885-894.
[40] H. Wadell, Volume, shape, and roundness of rock particles, The Journal of Geology, 40 (1932) 443-451.
[41] H. Wadell, Sphericity and roundness of rock particles, The Journal of Geology, 41 (1933) 310-331.
[42] W.C. Krumbein, Measurement and geological significance of shape and roundness of sedimentary particles, Journal of Sedimentary Research, 11 (1941) 64-72.
[43] C. Mora, A. Kwan, Sphericity, shape factor, and convexity measurement of coarse aggregate for concrete using digital image processing, Cement and concrete research, 30 (2000) 351-358.
[44] Y. Guo, J. Wang, V. Markine, G. Jing, Ballast mechanical performance with and without under sleeper pads, Ksce J Civ Eng, 24 (2020) 3202-3217.
[45] B. Indraratna, P.K. Thakur, J.S. Vinod, Experimental and numerical study of railway ballast behavior under cyclic loading, International Journal of Geomechanics, 10 (2010) 136-144.
[46] S.K.K. Hussaini, K. Sweta, Investigation of deformation and degradation response of geogrid-reinforced ballast based on model track tests, P I Mech Eng F-J Rai, 235 (2020) 505-517.
[47] T. Ngo, B. Indraratna, Analysis of deformation and degradation of fouled ballast: experimental testing and DEM modeling, International Journal of Geomechanics, 20 (2020).
[48] B. Indraratna, T. Ngo, C. Rujikiatkamjorn, Performance of ballast influenced by deformation and degradation: laboratory testing and numerical modeling, International Journal of Geomechanics, 20 (2020).
[49] T. Pan, E. Tutumluer, Evaluation of visual based aggregate shape classifications using the university of illinois aggregate image analyzer (UIAIA), in: GeoShanghai International Conference 2006, 2006.
[50] B. Indraratna, W. Salim, Deformation and degradation mechanics of recycled ballast stabilised with geosynthetics, Soils and Foundations, 43 (2003) 35-46.
[51] D. Li, J. Hyslip, T. Sussmann, S. Chrismer, Railway Geotechnics, CRC Press, 2015.
[52] W.D. Pye, M.H. Pye, Sphericity determinations of pebbles and sand grains, Journal of Sedimentary Research, Vol. 13 (1943).
[53] C.F. Mora, A.K.H. Kwan, Sphericity, shape factor, and convexity measurement of coarse aggregate for concrete using digital image processing, Cem. Concr. Res., 30 (2000) 351-358.
[54] C. Rao, E. Tutumluer, I.T. Kim, Quantification of coarse aggregate angularity based on image analysis, Transportation Research Record, 1787 (2002) 117-124.
[55] E.D. Sneed, R.L. Folk, Pebbles in the Lower-Colorado-River, Texas a Study in Particle Morphogenesis, J Geol, 66 (1958) 114-&.
[56] S.E. Gur Y, Livneh M., Effect of coarse-fraction flakiness on the strength of graded materials, in: Asian Conf Soil Mech & Fdn E Proc /Is/, 1967, pp. 276-281.
[57] H.C.M. D.R.Ahlbeck, R.H.Prause, The development of analytical models for railroad track dynamics, Proceedings of a Symposium Held at Princeton University, (1975) 239-263.
[58] J.M.S.a.M. Youldashkhan, Investigation on the accuracy of the current particles in analysis of railway track concrete sleepers, (2005).
[59] J.A. Zakeri, J. Sadeghi, Field investigation on load distribution and deflections of railway track sleepers, J Mech Sci Technol, 21 (2007) 1948-1956.

[60] J. Sadeghi, Field investigation on dynamics of railway track pre-stressed concrete sleepers, Advances in Structural Engineering, (2009).
[61] B. Zuada Coelho, M.A. Hicks, Numerical analysis of railway transition zones in soft soil, Proceedings of the Institution of Mechanical Engineers, Part F: Journal of Rail and Rapid Transit, 230 (2016) 1601-1613.
[62] C. Zhang, G. Jiang, Full-scale model testing of the dynamic response of lime-stabilized weathered red mudstone subgrade under railway excitation, Soil Dyn Earthq Eng, 130 (2020) 105999.
[63] G. Lombaert, G. Degrande, S. François, D.J. Thompson, Ground-borne vibration due to railway traffic: A review of excitation mechanisms, prediction methods and mitigation measures, Notes on Numerical Fluid Mechanics and Multidisciplinary Design, Springer Berlin Heidelberg, (2015) 253-287.
[64] Abadi, Taufan, L. Pen, A. Zervos and W. Powrie, Measuring the area and number of ballast particle contacts at sleeper/ballast and ballast/subgrade interfaces, International Journal of Railway Technology, 4 (2015) 45-72.
[65] E.T. Selig, J.M. Waters, Track geotechnology and substructure management, (1994).